

Supplement to ‘From dome to duplex: convergent gravitational collapse explains intracratonic dome and nappe tectonics, central Australia’

Youseph Ibrahim¹, Patrice F. Rey¹, Donna L. Whitney², Christian Teyssier², Françoise Roger³, Valérie Bosse⁴ and Bénédicte Cenki³

¹School of Geosciences, University of Sydney, NSW 2006, Australia

²Department of Earth Sciences, University of Minnesota, Minneapolis, Minnesota 55455, USA

³Géosciences Montpellier, Université de Montpellier, CNRS, Montpellier 34095 Cedex 5, France

⁴Laboratoire Magmas et Volcans, Campus Universitaire Des Cézeaux, 63178 Aubière Cedex, France.

FIELD PHOTOS

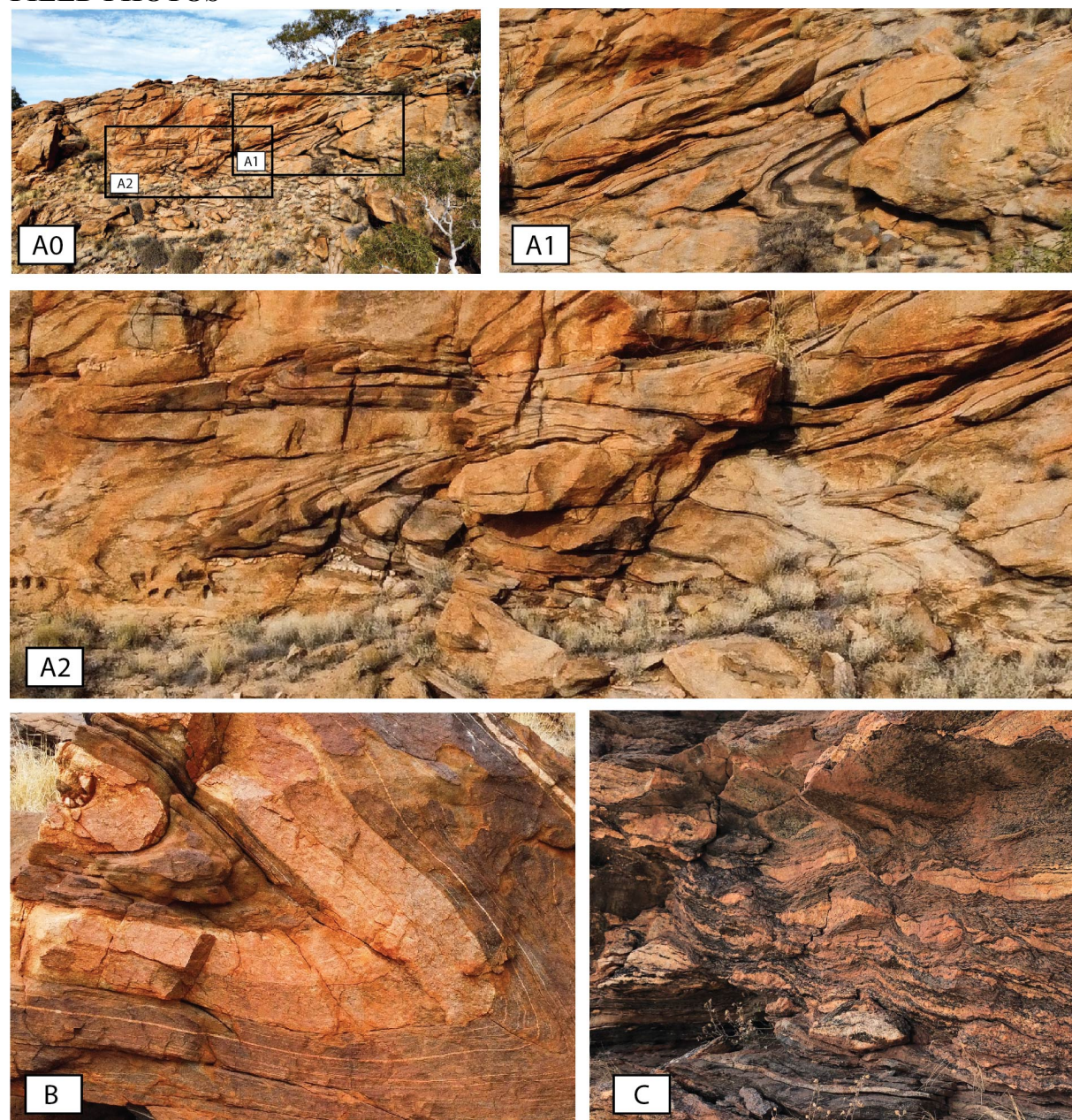
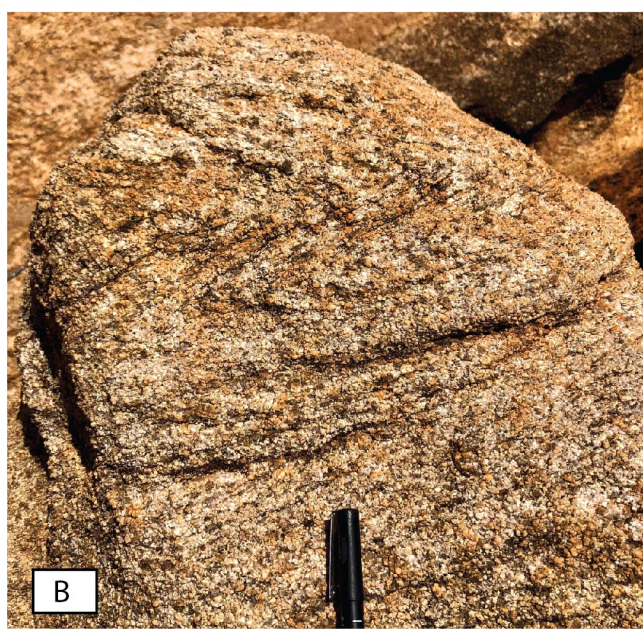


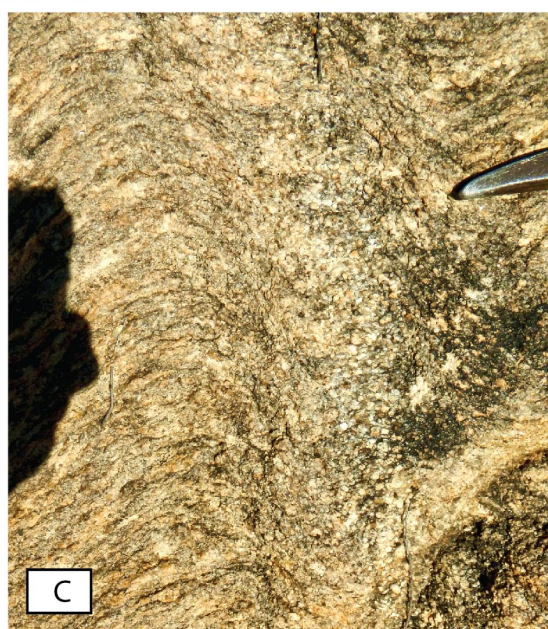
Figure S 1. (A0-2) Isoclinally folded migmatites folding a (B) pre-existing fabric and (C) asymmetric boudinage in migmatites a few meters on top of the Huckitta granodiorite.



A



B



C

Figure S 2 (A-B) Folded magmatic fabrics and (C) melt segregation.



Figure S 3. Folded leucocratic vein within the metatexite envelope of the Huckitta sub-dome.

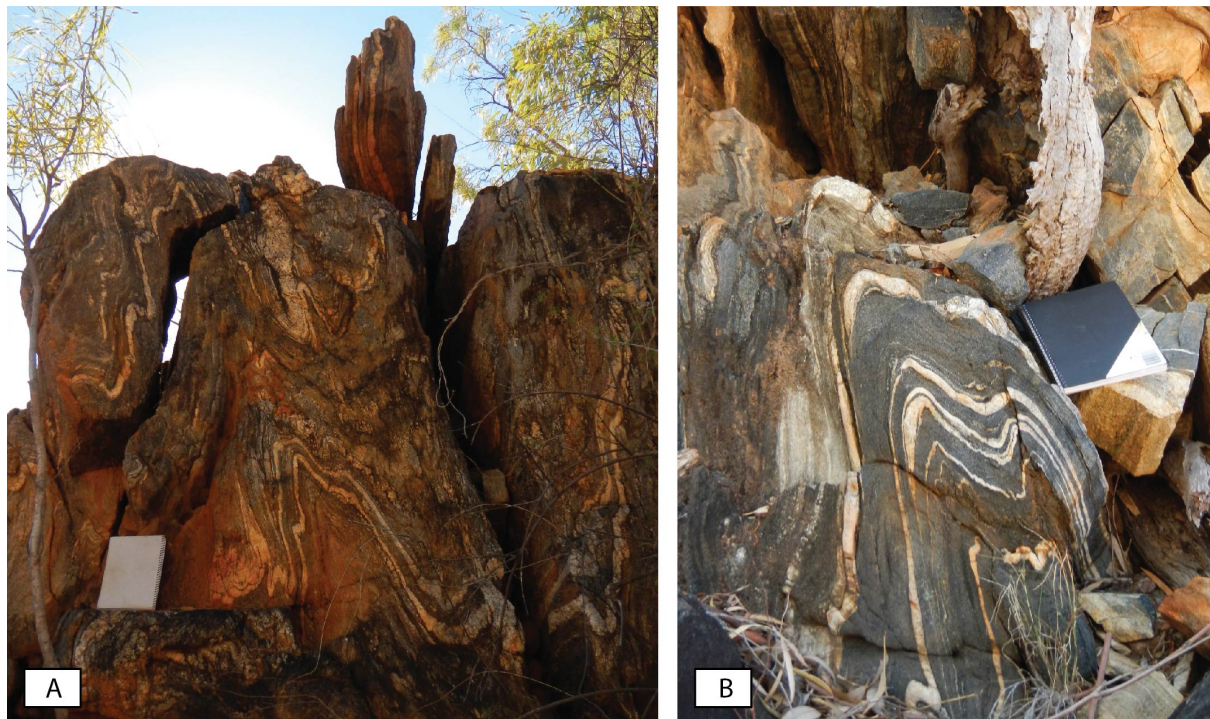


Figure S 4. Upright folds in the median high-strain zone between the Inkamulla and Huckitta sub-domes.

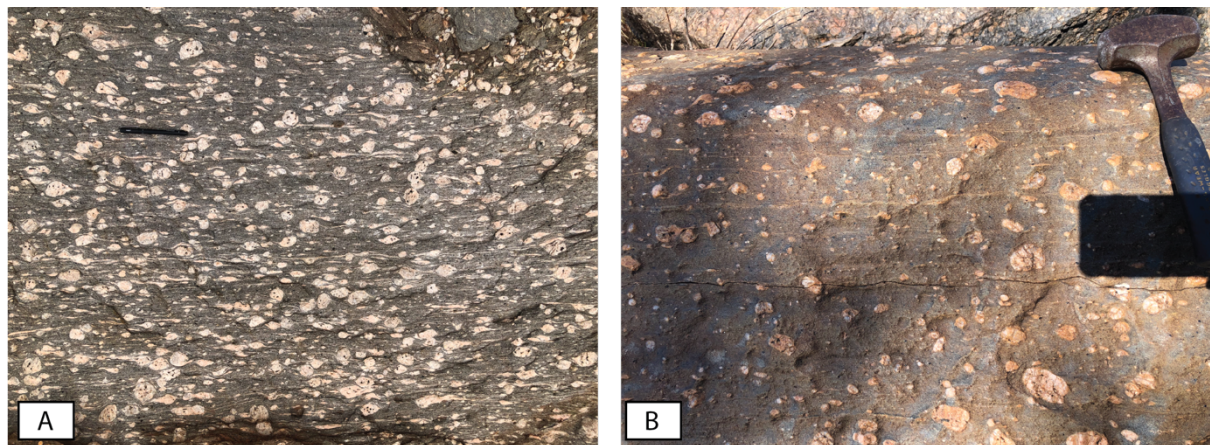


Figure S 5. Bruna Granitic Gneiss with large K-feldspar clasts embedded within a fine-grained matrix.

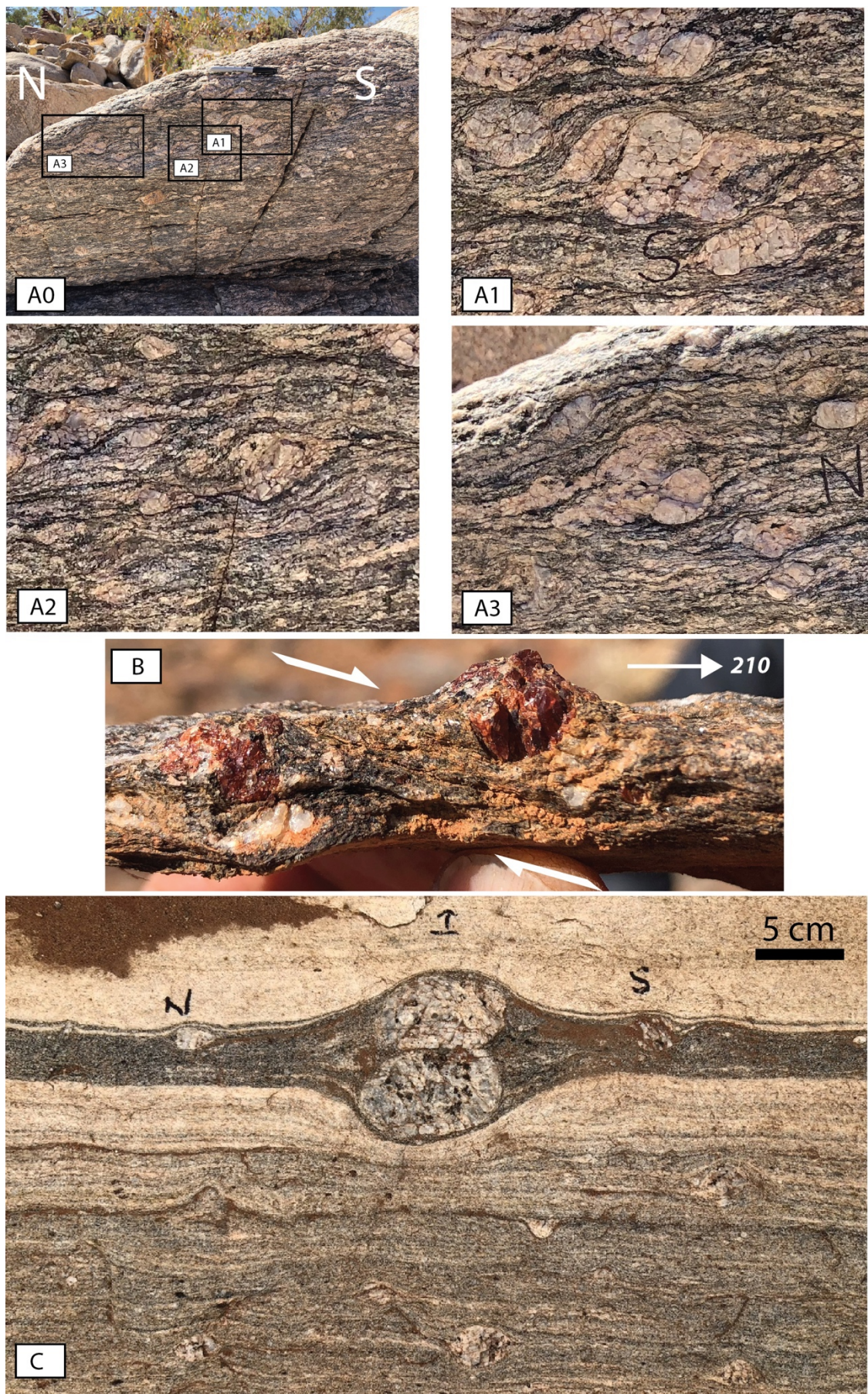


Figure S6. (A-B) Kinematic indicators on the X-Z plane including strain shadows and S-C fabrics showing top to the southwest sense of shear. (C) K-feldspar clast showing more complicated deformation with a large pure shear component.

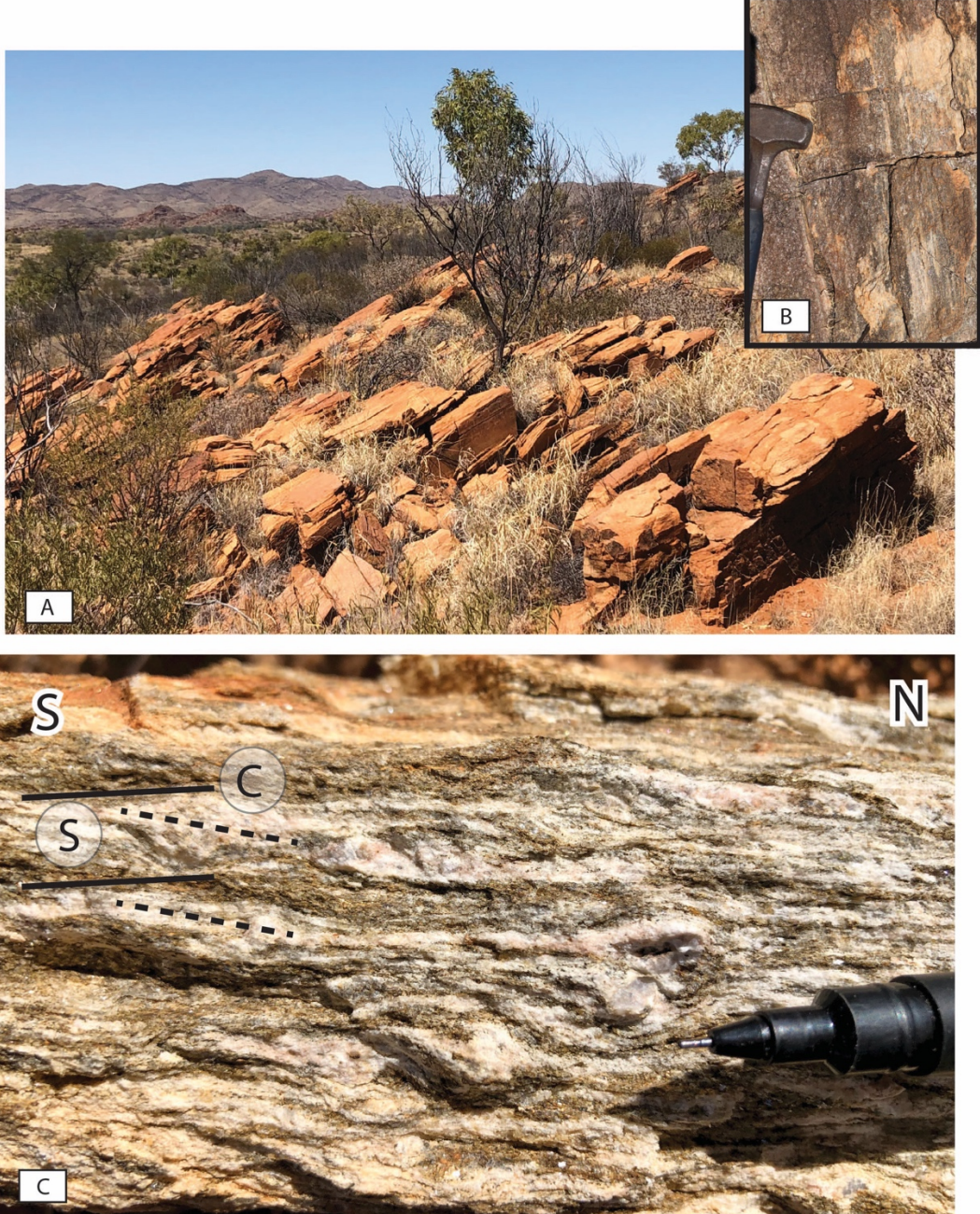


Figure S 7. (A) North dipping Illogwa shear zone looking to the East. (B) LS fabric with muscovite-bearing down-dip lineation with (C) top to the south kinematics.

GEOCHRONOLOGY

Analytical Methods

Monazite and titanite were analysed in-situ in thin section to preserve the textural relationships between accessory minerals, mineralogical assemblage, and the fabric. Before analysis, backscatter electron (BSE) images were acquired for all grains using a scanning electron microscope (SEM) to check spot positions with respect to the internal microstructures, inclusions, fractures, or other physical defects.

U-Th-Pb geochronology on monazite and titanite was conducted by LA-ICPMS at the Laboratoire Magmas et Volcans, Clermont-Ferrand (France). The analyses involved ablation of grains with a Resonetics Resolution M-50 powered by an ultra-short pulse ATL Atlex Excimer laser system operating at a wavelength of 193 nm coupled with an Agilent 8900 triple quadrupole ICP-MS. Data reduction was carried out with the GLITTER® software package from Macquarie Research Ltd (van Achterbergh et al., 2001). Dates and diagrams were generated using Isoplot/Ex v. 2.49 software package (Ludwig, 2001). All uncertainties are given at $\pm 2\sigma$.

Monazite and titanite were also analysed in situ on thin section to preserve the textural relationships between accessory minerals, mineralogical assemblage, and the fabric. Before analysis, backscatter electron (BSE) and cathodoluminescence (CL) images were acquired for each grain using a scanning electron microscope (SEM), the locations of LA-ICPMS spot were selected based on the internal microstructures and to avoid inclusions, fractures, and other physical defects.

U-Th–Pb isotope data of monazite and titanite were obtained at the LMV, Clermont-Ferrand, France, by LA-ICPMS. The analytical method for isotope dating with LA-ICPMS is similar to that reported in Paquette and Tiepolo (2007), Hurai et al. (2010) and Paquette et al. (2014).

The analyses involved the ablation of minerals with a Resonetics M-50 laser system operating at a wavelength of 193 nm (Müller et al., 2009). For monazite and titanite, spot diameters of 12 μm and 33 μm were used, associated with repetition rates of 1 Hz and 3 Hz, and laser fluences of 2.87 J/cm² and 2.65 J/cm², respectively. The ablated material was carried in helium and then mixed with nitrogen and argon before injection into the plasma source of an Agilent 8900 triple quadrupole ICP-MS. The alignment of the instrument and mass calibration were performed before each analytical session using the NIST SRM612 reference glass by inspecting the signal of ²³⁸U and by minimizing the ThO⁺/Th⁺ ratio (<1%). Raw data were corrected for U and Pb fractionation during laser sampling and for instrumental mass bias by standard bracketing with repeated measurements of the Trebilcock monazite (Tomasca, 1996). For the titanite analyses, owing to a lack of high-quality titanite natural standards (i.e. negligible common Pb), 91500 zircon standard was used (Table DB1) (Wiedenbeck et al., 1995). The reproducibility and accuracy of the corrections were controlled by repeated analyses of the Bananeira monazite or MKED1 and Khan titanite standards (Gonçalves et al., 2016; Spandler et al., 2016; Heaman, 2009) treated as unknown (Table DB1). For monazite and titanite, because of the non-negligible mercury content of the Ar gas creating an isobaric interference between ²⁰⁴Pb and ²⁰⁴Hg, no common Pb correction was applied prior to data reduction using the GLITTER® software package (van Achterbergh et al., 2001). The detailed analytical procedures are presented in Table DB1. The calculated ratios were exported, and ages and diagrams generated using Isoplot/Ex v. 2.49 software package (Ludwig, 2001). The decay constants used for the U–Pb system are those determined by Jaffey et al. (1971) and recommended by the IUGS (Steiger & Jäger, 1977). Analytical results are given in Table DB2-3. In the text, tables and figures, all uncertainties are given at 2σ level.

Discordant data analysed by the LA-ICPMS method are considered only if they allow for the definition of discordia lines in the concordia or/and Tera Wasserburg diagrams, so that the age(s) by (lower and/or upper) intercept(s) have geological significance. Otherwise, the interpretation of the discordant data remains too doubtful. In LA-ICPMS analyses, several factors that are difficult to detect from the inspection of the time-resolved signals might contribute to discordance (e.g., common Pb, by way of inclusions, mixture of two components of distinct age, small cracks).

Results

The field location of the two samples dated (Fig. S9) is shown in Fig. 1 and coordinates are provided in Table S1. Monazite grains in sample CA1938 can be either included in biotite or muscovite or present in the quartzo-feldspathic matrix. Monazite crystals are abundant, most of them are less than 50 μm in size but with a few up to $\sim 100 \mu\text{m}$. Although some grains show weak concentric or patchy zoning in response to BSE, most do not show a zoning. Twenty-five spots on fourteen monazites grains were performed (Table S2). Of these analyses, six were excluded from age calculation because they are moderately to strongly discordant (93-61 % of concordance), probably due to minor or less minor incorporation of common Pb (Fig. S7 A). The remaining analyses ($\geq 95\%$ of concordance) show $^{206}\text{Pb}/^{238}\text{U}$ dates between 365 and 309 Ma. Plotted in a histogram and Tera-Wasserburg diagram (Fig S7 A-B), the data highlights the presence of at least two distinct populations, one at ~ 340 Ma (grey ellipses) and another at ~ 315 Ma (green ellipses), as well as a concordant date at 365 ± 7 Ma (blue ellipse) (Table S2 and Fig. S7 B). There is no correlation between the dates and the textural position of the monazites. The weighted average $^{206}\text{Pb}/^{238}\text{U}$ date of the youngest population is 314 ± 4 (MSWD = 0.85; N =5). This population has a rather homogeneous and high range of Th (around 45000 ppm) U (around 11000 ppm) and Pb (around 1250 ppm) contents with a low Th/U ratio ranging from 5.1 to 3.7 (Table S2). The oldest population consists of eleven datapoints among which four seem to have been affected by a mixing of the two zones at 340 Ma and 314 Ma and by low common Pb contamination (dotted grey ellipses), the weighted average $^{206}\text{Pb}/^{238}\text{U}$ date obtained on this population is 339 ± 4 Ma (MSWD = 1.4; N =7/11). Their high concentrations in Th, U and Pb are more heterogeneous, and their Th/U ratios are also very variable between 23.9 and 4.7 highlighting the lack of correlation between the Th/U ratio and the dates.

Titanite grains in sample CA1918 are abundant, and medium size (100 – 400 μm). The BSE images show titanite without discernible internal zoning. Thirty-six analyses on twenty-six titanites were performed. Most of them have low Pb (<8 ppm), U (ca. 145-18 ppm) and Th (ca. 17-3 ppm) contents and very low Th/U ratios between 0.27 and 0.05 (Table S YY). The Tera Wasserburg diagram displays discordant data with a percentage of concordance ranging from 39 to 70 % due to a relative high proportion of common Pb and with a dispersion of $^{206}\text{Pb}/^{238}\text{U}$ dates between ~ 397 and 326 Ma (Table S3; Fig. S7 C). The linear regression yields a lower intercept of 315 ± 4 Ma (MSWD = 0.85; N = 30) and a $^{207}\text{Pb}/^{206}\text{Pb}$ initial value of 0.85 ± 0.04 consistent with the composition of the Variscan common Pb (c.a. 0.856) following the model of Stacey and Kramers (1975) for the terrestrial Pb evolution. Moreover, we have applied a ^{207}Pb -based common Pb correction to the U-Pb dataset using the common-Pb composition from the two-stage crustal evolution model of Stacey and Kramers (1975). The corrected dates are between 329 and 302 Ma (Table S3) with a weighted average of 315 Ma ± 2 Ma (MSWD =1.7; N = 30) (Fig. S7 D). These two dates are similar. The 315 Ma age obtained on the titanites from the aplite CA1918 is interpreted as the minimum emplacement age of the dyke.

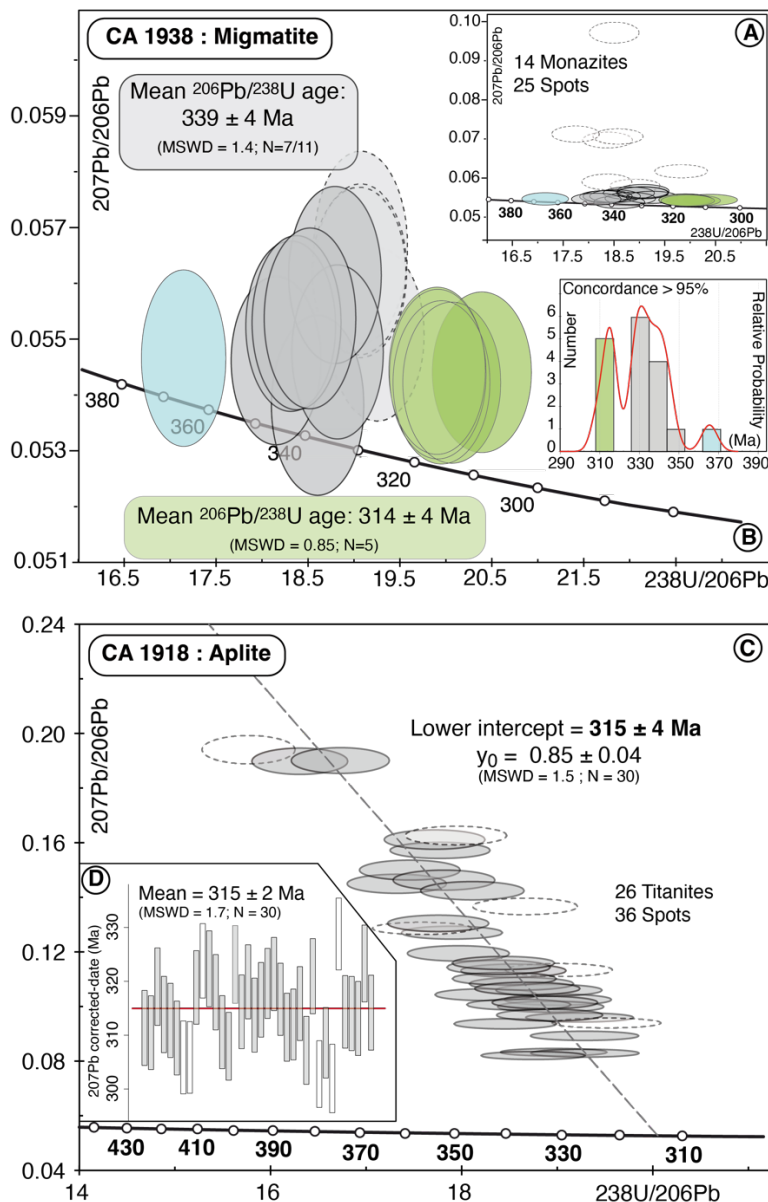


Figure S 8. U-Pb monazite and titanite diagrams obtained by LA-ICPMS on thin section. A and B: Monazite U-Th-Pb Tera-Wasserburg diagrams on the migmatite (sample CA1938) of the Median High strain zone. Error ellipses and uncertainties in ages are $\pm 2\sigma$ level. Dotted white ellipses are discordant data and are not considered in the histogram diagram (B) and for the age calculations, while dotted grey ellipses are not considered only when calculating the concordia age. C: Titanite U-Th-Pb Tera Wasserburg diagram from the aplite (CA1918). D: The weighted average of 207-corrected dates diagram. Error ellipses and uncertainties in ages are $\pm 2\sigma$ level. Dotted white ellipses and boxes are not taken into account for the age calculation.

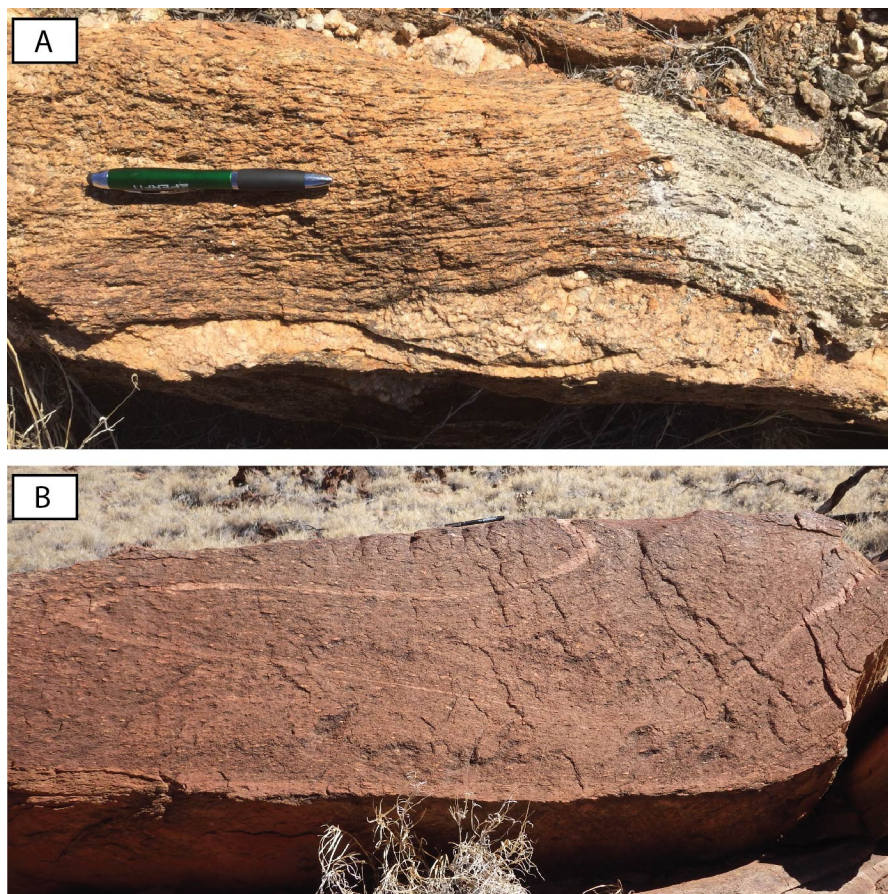


Figure S 9. (A) Field photo of CA1938 (Monazite), a leucosome in a metatexite. (B) Field photo of sample CA1918 (Titanite), a folded aplite vein axial planar to the foliation in the hosting Bruna Granitic Gneiss, within the Bruna décollement zone.

Table S 1. Operating conditions and instrument settings for U-Pb analyses

Sample Location		
CA1938 (Monazite)	135.22325, -23.10451	
CA1918 (Titanite)	135.32518, -23.20719	
Laboratory & Sample Preparation		
Laboratory name	Laboratoire Magmas & Volcans, Clermont-Ferrand, France	
Sample type/mineral	Monazite and titanite	
Sample preparation	thin section (Université Montpellier)	
Imaging	CL, FEI QUANTA 200, 15 kV, 15 mm working distance (Université Montpellier)	
Laser ablation system		
Make, Model & type	Resonetech/M-50E 193nm, Excimer	
Ablation cell & volume	Laurin Cell ® two volumes cell, Laurin Technic Ltd., volume ca. 1-2 cm ³	
Laser wavelength	193 nm	
Pulse width	< 4 ns	
Fluence	Titanite: 2.65 J.cm ⁻²	Monazite : 2.87 J.cm ⁻²
Repetition rate	3 Hz	1 Hz
Spot size	33 µm	12 µm
Sampling mode / pattern	Single spot	
Carrier gas	100% He, Ar make-up gas and N ₂ combined using the Squid® device from RESolution Instruments.	
Background collection	30 secs	
Ablation duration	60 secs	
Wash-out delay	30 secs	
Cell carrier gas flow	0.75 l/min	
ICP-MS Instrument		
Make, Model & type	Agilent 8900 QQQ-ICP-MS	
Sample introduction	Via conventional tubing	
RF power	1350W	
Make-up gas flow	0.87 l/min Ar	
Detection system	Single collector secondary electron multiplier	
Masses measured	204, 206, 207, 208, 232, 238	
Integration time per peak	10 ms	
Total integration time per reading	130 ms <i>(should represent the time resolution of the data)</i>	
Sensitivity / Efficiency	800000 cps/ppm ²³⁸ U (47 µm, 10Hz)	
Dead time	35 ns	
Data Processing		
Gas blank	30 second on-peak	
Calibration strategy	Titanite: 91500 zircon used as primary reference material, MKED1 and Khan titanite standards used as secondary reference material (Quality Control)	Monazite: Trebilcock used as primary reference material, Bananeira used as secondary reference materials (Quality Control)
Reference Material info	91500 Zircon (Wiedenbeck et al., 1995) MKED1 Titanite (Spandler et al., 2016) Khan titanite (Heaman, 2009)	Monazite: Trebilcock (Tomascak, 1996) Bananeira (Gonçalves et al., 2016)

Data processing package used / Correction for LIEF	GLITTER ® (van Achterbergh et al., 2001)
Mass discrimination	Standard-sample bracketing with $^{207}\text{Pb}/^{206}\text{Pb}$ and $^{206}\text{Pb}/^{238}\text{U}$ normalized to reference material 91500 or Trebilcock
Common-Pb correction, composition and uncertainty	No common-Pb correction.
Uncertainty level & propagation	Ages are quoted at 2sigma absolute, propagation is by quadratic addition according to Horstwood et al. (2003). Reproducibility and age uncertainty of reference material are propagated.
Quality control / Validation	Titanite: MKED1: $^{207}\text{Pb}/^{206}\text{Pb}$ age = 1524 ± 6 (2SD; MSWD = 2.1; N=21) Khan : Lower intercept = 513 ± 4 Ma (2SD, MSWD = 1.3, N = 9) Monazite: Bananeira: $^{207}\text{Pb}/^{235}\text{U}$ age = 501.3 ± 3.8 Ma (2SD; MSWD = 0.67; N=13)
Other information	For detailed method description see Paquette and Tiepolo (2007), Hurai et al. (2010), Paquette et al. (2014). For detailed laser technical description see Müller et al. (2009).

Table S2. Analytical results of monazite analysis

	Content (ppm)			Uncorrected Ratios (a)							(b)		Age (Ma)				207Pb-Corrected			
	Analysis #	Pb	Th	U	Th/U	Pb207/U235	±2σ	Pb206/U238	±2σ	Rho	conc%	Pb207/U235	±2σ	Pb206/U238	±2σ	date (c)	± 2σ			
Mnz1-a	Bt	1112	59687	2956	20.2	0.399	0.013	0.0538	0.0012	0.67	99	341	11	338	7	338	7			
Mnz1-b	Bt	1167	57654	5220	11.0	0.415	0.013	0.0551	0.0012	0.70	98	352	11	346	8	345	7			
Mnz2	Bt-Matrix	777	36061	3430	10.5	0.440	0.014	0.0583	0.0013	0.68	99	370	12	365	8	365	8			
Mnz10-2	Bt-Matrix	721	35526	3448	10.3	0.412	0.013	0.0540	0.0012	0.68	97	351	11	339	7	338	7			
Mnz11	Bt-Matrix	1355	53345	12508	4.3	0.368	0.011	0.0490	0.0011	0.71	97	318	10	309	7	308	7			
Mnz9	Bt	1002	45141	5619	8.0	0.416	0.013	0.0546	0.0012	0.69	97	353	11	343	7	342	7			
Mnz12-2-a	Matrix	991	48768	4485	10.9	0.412	0.013	0.0532	0.0012	0.69	95	350	11	334	7	333	7			
Mnz12-2-b	Matrix	402	15928	2933	5.4	0.523	0.017	0.0544	0.0012	0.68	80	427	14	342	7	335	7			
Mnz12-1	Bt-Matrix	1000	39784	8465	4.7	0.407	0.013	0.0525	0.0011	0.71	95	347	11	330	7	329	7			
Mnz13-2	Bt	832	38673	5317	7.3	0.394	0.012	0.0519	0.0011	0.69	97	338	11	326	7	325	7			
Mnz13-3	Bt	718	31692	4887	6.5	0.401	0.013	0.0531	0.0011	0.68	97	343	11	334	7	333	7			
Mnz8-2-a	Bt	1212	68991	2881	23.9	0.409	0.014	0.0524	0.0011	0.66	95	349	12	329	7	328	7			
Mnz8-2-b	Bt	978	41778	7669	5.4	0.429	0.013	0.0505	0.0011	0.69	87	363	11	317	7	314	7			
Mnz8-3	Bt	1206	45214	12071	3.7	0.373	0.011	0.0498	0.0011	0.71	97	322	10	314	7	313	7			
Mnz7	Bt-Matrix	539	23576	3719	6.3	0.724	0.023	0.0540	0.0012	0.69	61	553	17	339	7	321	7			
Mnz6-4	Matrix	868	37555	7304	5.1	0.377	0.012	0.0502	0.0011	0.69	97	325	10	316	7	315	7			
Mnz6-2	Bt-Matrix	672	30733	4333	7.1	0.438	0.014	0.0510	0.0011	0.67	87	369	12	321	7	317	7			
Mnz6-1	Ms	1185	45044	11841	3.8	0.375	0.012	0.0501	0.0011	0.70	98	323	10	315	7	315	7			
Mnz6-3	Ms	1082	55616	5065	11.0	0.524	0.017	0.0538	0.0012	0.69	79	428	13	338	7	331	7			
Mnz3-1	Bt	858	36567	6822	5.4	0.423	0.013	0.0529	0.0011	0.68	93	358	11	332	7	330	7			
Mnz3-2	Ms	269	10899	1730	6.3	0.443	0.016	0.0545	0.0012	0.62	92	373	13	342	7	340	7			
Mnz4-2-a	Matrix	1149	46811	10251	4.6	0.377	0.012	0.0502	0.0011	0.69	97	325	10	316	7	315	7			
Mnz4-2-b	Matrix	1444	80082	3835	20.9	0.554	0.018	0.0564	0.0012	0.67	79	447	14	353	8	346	7			
Mnz5-a	Bt	2671	150201	6974	21.5	0.415	0.013	0.0544	0.0012	0.68	97	352	11	342	7	341	7			
Mnz5-b	Bt	2945	160376	9558	16.8	0.406	0.013	0.0524	0.0011	0.69	95	346	11	329	7	328	7			

a: Ratios are corrected for U-Pb fractionation and for instrumental mass bias but uncorrected from common Pb

b: % conc = percentage of concordance= $((206\text{Pb}/238\text{U})\text{age} / (207\text{Pb}/235\text{U})\text{age}) \times 100$ c: $(206\text{Pb}/238\text{U})$ date corrected by a 207Pb-based common Pb correction using the common-Pb composition from the two-stage crustal evolution model of Stacey and Kramers (1975)

Table S3. Analytical results of titanite analysis

	Content (ppm)			Uncorrected Ratios (a)							(b)	Age (Ma)				207Pb-Corrected		
	Pb	Th	U	Th/U	Pb207/U235	±2σ	Pb206/U238	±2σ	Rho	conc%	Pb207/U235	±2σ	Pb206/U238	±2σ	date (c)	±2σ		
Tnt 1-1	5.6	6.7	104.5	0.06	0.638	0.018	0.0519	0.0012	0.84	65	501	14	326	8	312	7		
Tnt 1-2	4.5	5.4	78.4	0.07	0.744	0.022	0.0526	0.0013	0.83	59	565	16	331	8	310	7		
Tnt 3-1	7.8	12.1	144.9	0.08	0.605	0.017	0.0527	0.0013	0.87	69	481	13	331	8	319	7		
Tnt 3-2	6.9	12.4	129.1	0.10	0.593	0.017	0.0518	0.0012	0.86	69	473	13	326	8	314	7		
Tnt 2	4.6	6.7	80.9	0.08	0.728	0.021	0.0528	0.0013	0.83	60	555	16	332	8	313	7		
Tnt 4	6.5	12.1	115.8	0.10	0.688	0.019	0.0520	0.0012	0.86	61	532	15	327	8	310	7		
Tnt 6	5.1	9.6	93.3	0.10	0.664	0.019	0.0512	0.0012	0.84	62	517	15	322	8	306	7		
Tnt 5	3.5	4.1	59.8	0.07	0.822	0.024	0.0526	0.0013	0.81	54	609	18	330	8	306	7		
Tnt 7	4.2	6.4	63.7	0.10	0.979	0.028	0.0559	0.0014	0.85	51	693	20	351	8	319	7		
Tnt 8-1	6.0	11.3	89.6	0.13	1.009	0.028	0.0569	0.0014	0.86	50	708	20	357	9	324	7		
Tnt 8-2	4.0	6.6	66.7	0.10	0.788	0.023	0.0548	0.0013	0.82	58	590	17	344	8	322	7		
Tnt 9-1	4.6	5.1	79.8	0.06	0.747	0.021	0.0538	0.0013	0.83	60	566	16	338	8	318	7		
Tnt9-2	4.3	3.9	75.0	0.05	0.773	0.022	0.0529	0.0013	0.82	57	581	17	332	8	311	7		
Tnt 11	3.9	8.4	54.5	0.15	1.219	0.035	0.0563	0.0014	0.84	44	810	23	353	8	308	7		
Tnt 10-1	7.3	15.2	133.9	0.11	0.604	0.017	0.0533	0.0013	0.85	70	480	13	335	8	323	7		
Tnt 10-2	3.9	12.1	64.6	0.19	0.802	0.024	0.0537	0.0013	0.81	56	598	18	337	8	314	7		
Tnt 12-1	2.8	9.5	41.2	0.23	1.013	0.031	0.0563	0.0014	0.79	50	710	22	353	9	320	7		
Tnt 12-2	3.6	9.4	58.6	0.16	0.841	0.025	0.0539	0.0013	0.81	55	620	18	339	8	314	7		
Tnt 13-1	4.1	16.7	66.0	0.25	0.824	0.024	0.0542	0.0013	0.82	56	610	18	340	8	316	7		
Tnt 13-2	1.7	3.7	20.3	0.18	1.603	0.052	0.0613	0.0015	0.77	39	972	32	383	10	320	6		
Tnt 14	2.4	5.3	32.9	0.16	1.154	0.036	0.0577	0.0014	0.78	46	779	24	362	9	321	7		
Tnt 15-1	2.2	6.0	31.2	0.19	1.184	0.037	0.0573	0.0014	0.78	45	793	25	359	9	317	7		
Tnt 15-2	1.8	3.7	21.5	0.17	1.565	0.050	0.0597	0.0015	0.78	39	956	31	374	9	311	6		
Tnt 16	2.2	5.2	32.1	0.16	1.132	0.036	0.0561	0.0014	0.77	46	769	25	352	9	312	7		
Tnt 17	3.6	13.4	57.4	0.23	0.858	0.026	0.0544	0.0013	0.79	54	629	19	341	8	316	7		
Tnt 18	3.1	11.0	40.7	0.27	1.254	0.038	0.0564	0.0014	0.80	43	825	25	354	9	307	6		
Tnt 19-1	3.2	10.0	48.8	0.20	0.917	0.028	0.0557	0.0014	0.78	53	661	20	349	8	321	7		
Tnt 19-2	3.3	6.6	45.9	0.14	1.250	0.037	0.0557	0.0014	0.82	42	823	24	350	8	303	6		
Tnt 20	2.8	7.6	40.6	0.19	1.084	0.034	0.0552	0.0013	0.79	46	746	23	346	8	309	6		
Tnt 21	3.4	3.6	52.8	0.07	1.010	0.030	0.0536	0.0013	0.80	47	709	21	336	8	302	6		
Tnt 22	1.6	1.6	18.6	0.08	1.697	0.057	0.0635	0.0016	0.76	39	1008	34	397	10	329	7		
Tnt 23-1	4.8	9.5	76.8	0.12	0.867	0.025	0.0542	0.0013	0.82	54	634	18	341	8	314	7		
Tnt 23-2	4.4	10.2	72.6	0.14	0.786	0.023	0.0535	0.0013	0.81	57	589	18	336	8	314	7		
Tnt 24	4.2	9.3	71.7	0.13	0.741	0.022	0.0530	0.0013	0.79	59	563	17	333	8	313	7		
Tnt 25	6.5	27.4	108.1	0.25	0.700	0.020	0.0542	0.0013	0.83	63	539	16	340	8	323	7		
Tnt 27	4.5	9.2	78.8	0.12	0.706	0.021	0.0529	0.0013	0.80	61	542	16	332	8	314	7		

a: Ratios are corrected for U-Pb fractionation and for instrumental mass bias but uncorrected from common Pb

b: % conc = percentage of concordance= $((206\text{Pb}/238\text{U})_{\text{age}} / (207\text{Pb}/235\text{U})_{\text{age}}) \times 100$ c: $(206\text{Pb}/238\text{U})$ date corrected by a 207Pb-based common Pb correction using the common-Pb composition from the two-stage crustal evolution model of Stacey and Kramers (1975)

STRUCTURAL DATA

Table S 4. Lineation measurements and GPS coordinates in decimal degree format.

Lon	Lat	Plunge Direction	Plunge	Lon	Lat	Plunge Direction	Plunge
134.96076	-23.4501	308	36	135.29224	-23.09519	31	23
134.99304	-23.439412	165	25	135.29028	-23.09241	17	19
134.97598	-23.477184	346	11	135.28561	-23.08622	20	24
134.970392	-23.485811	190	15	135.07647	-23.26981	28	32
135.177601	-23.103101	30	13	135.26901	-23.07987	27	43
135.177601	-23.103101	10	34	135.26469	-23.07717	30	29
135.27859	-23.07548	50	38	135.26077	-23.07998	36	15
135.28348	-23.07169	66	50	135.26111	-23.07813	18	12
135.24269	-23.37912	22	11	135.25627	-23.07993	35	22
135.22151	-23.38827	50	32	135.32256	-23.18232	12	27
135.22144	-23.3883	35	22	135.32359	-23.18212	105	18
135.31885	-23.33761	94	19	135.32211	-23.1817	15	20
135.27806	-23.32424	84	18	135.29857	-23.11884	40	12
135.27806	-23.32424	74	21	135.29004	-23.11304	145	17
135.25909	-23.36409	25	45	135.29091	-23.11569	24	28
135.247475	-23.37615	32	44	135.29178	-23.11838	43	37
135.37909	-23.37909	32	10	135.2962	-23.11691	37	8
135.23834	-23.36762	24	21	135.29356	-23.11953	35	18
135.229736	-23.366566	21	19	135.29871	-23.12017	42	14
135.220995	-23.391575	14	31	135.06705	-23.11612	330	5
135.218685	-23.302111	10	24	135.06807	-23.11563	152	1
135.21451	-23.396635	18	18	135.13286	-23.09922	54	2
135.2106	-23.40958	16	20	135.13368	-23.09847	108	28
135.26698	-23.26622	35	13	135.15813	-23.09461	214	14
135.26698	-23.26622	26	10	135.16301	-23.09525	168	49
135.23643	-23.24107	218	31	135.17758	-23.10253	29	10
135.23657	-23.4032	30	194	135.19267	-23.10098	355	12
135.23888	-23.23713	215	32	135.09884	-23.09884	345	35
135.23888	-23.23713	220	40	135.16118	-22.98343	35	33
135.23947	-23.22404	224	45	135.15395	-23.00364	358	26
135.27559	-23.36785	36	15	135.16753	-23.09624	220	9
135.22698	-23.10543	25	40	135.10069	-23.09486	221	9
135.22808	-23.10638	42	40	135.08121	-23.10149	220	12
135.22953	-23.10698	80	58	135.0593	-23.14141	133	16
135.23347	-23.11127	26	10	135.05969	-23.1414	150	10
135.23942	-23.11487	45	20	135.22685	-23.03285	0	55
135.23858	-23.11672	50	20	135.22784	-23.03455	339	42
135.24258	-23.12095	25	12	135.22508	-23.03571	20	46
135.24442	-23.12145	21	25	135.2251	-23.03512	22	42
135.25392	-23.12178	28	24	135.22368	-23.03065	342	26
135.15751	-23.0477	28	14	135.22449	-23.02919	320	19
135.22645	-23.03278	5	40	135.22627	-23.02975	167	20
135.1865	-23.05482	25	30	135.22647	-23.03002	47	40
135.20863	-23.06095	28	30	135.22754	-23.03065	6	36
135.21777	-23.0565	5	31	135.22606	-23.03129	354	48
135.23803	-23.05657	10	35	135.16563	-22.98071	328	55
135.25277	-23.0709	30	32	135.16606	-22.98043	15	39
135.16148	-23.09473	35	42	135.1664	-22.98098	340	43
135.13757	-23.09353	220	8	135.17491	-22.98513	10	20
135.11578	-23.10213	220	25	135.17578	-22.98589	9	29
135.08005	-23.1021	330	9	135.2773	-23.07825	55	45

135.07523	-23.1057	256	5	135.27686	-23.07681	54	54
135.17647	-23.10747	22	10	135.18811	-23.05322	57	46
135.17472	-23.10752	300	19	135.14473	-22.98537	259	20
135.1728	-23.10828	195	12	135.14163	-22.98783	336	10
135.17325	-23.11058	205	15	135.159	-23.04841	0	20
135.17475	-23.10973	210	15	135.15846	-23.04839	356	34
135.15956	-22.9746	2	76	135.21503	-23.09085	345	39
135.16556	-22.98072	335	42	135.21503	-23.09085	25	20
135.15869	-23.04809	5	12	135.21272	-23.08966	26	29
135.20805	-23.04235	350	43	135.18582	-23.11094	245	9
135.20964	-23.02833	354	29	135.1859	-23.11258	280	8
135.20911	-23.08394	0	28	135.18604	-23.11543	230	2
135.20961	-23.09257	328	40	134.90935	-23.32015	14	9
135.16815	-23.09826	145	0	134.91324	-23.31923	176	0
135.17172	-23.09986	107	7	134.91295	-23.31774	0	10
135.18013	-23.07175	15	5	135.31477	-23.14333	342	40
135.29356	-23.09729	315	0	135.32272	-23.1824	19	20
135.31306	-23.13826	30	15	135.32758	-23.19092	69	39
135.2959	-23.10252	0	18	135.32578	-23.21247	45	23
135.23593	-23.11353	24	14	135.32518	-23.20719	243	21
135.23212	-23.11037	30	24	135.35674	-23.19855	64	24
135.23116	-23.10786	15	12	135.22789	-23.03326	355	39
135.23108	-23.10583	44	22	135.08025	-23.09524	11	9
135.23184	-23.10454	38	26	135.07787	-23.0862	205	12
135.23184	-23.10442	28	19	135.07611	-23.08106	154	38
135.23195	-23.10132	18	38	135.22835	-23.09599	0	40
135.2298	-23.09992	176	40				

Table S 5. Foliation measurements and GPS coordinates in decimal degree format.

Lon	Lat	Strike	Dip	Lon	Lat	Strike	Dip
134.96076	-23.4501	230	60	135.07647	-23.26981	298	23
134.97598	-23.477184	288	32	135.26901	-23.07987	340	31
135.177601	-23.103101	10	14	135.26469	-23.07717	18	72
135.177601	-23.103101	314	18	135.26077	-23.07998	14	65
135.28348	-23.07169	330	54	135.26111	-23.07813	278	56
135.24269	-23.37912	285	19	135.25627	-23.07993	33	82
135.22328	-23.38878	0	54	135.25209	-23.08026	38	72
135.22151	-23.38827	324	36	135.24629	-23.08348	44	65
135.22144	-23.3883	327	19	135.23523	-23.08847	242	86
135.22144	-23.3883	315	25	135.32256	-23.18232	315	32
135.31885	-23.33761	67	25	135.32359	-23.18212	82	39
135.27806	-23.32424	54	35	135.32211	-23.1817	334	26
135.27806	-23.32424	50	26	135.29857	-23.11884	344	20
135.27806	-23.32424	50	42	135.2896	-23.11206	29	60
135.25909	-23.36409	325	50	135.29004	-23.11304	90	25
135.25909	-23.36409	324	30	135.29091	-23.11569	355	46
135.247475	-23.37615	1	52	135.29178	-23.11838	14	47
135.246541	-23.376013	350	50	135.29405	-23.11923	280	33
135.37909	-23.37909	316	11	135.29489	-23.11913	35	85
135.23834	-23.36762	323	34	135.2962	-23.11691	328	24
135.229736	-23.366566	14	29	135.29356	-23.11953	335	34
135.229736	-23.366566	312	34	135.29871	-23.12017	332	28
135.220995	-23.391575	134	46	135.06252	-23.12675	162	28
135.218685	-23.302111	314	22	135.06705	-23.11612	175	32
135.21451	-23.396635	301	24	135.06807	-23.11563	152	21
135.2106	-23.40958	284	26	135.13286	-23.09922	240	29
135.26698	-23.26622	320	12	135.13368	-23.09847	29	29

135.26698	-23.26622	300	14	135.15813	-23.09461	159	20
135.23643	-23.24107	64	52	135.16301	-23.09525	126	80
135.23643	-23.24107	65	48	135.17758	-23.10253	308	18
135.23657	-23.4032	96	35	135.19267	-23.10098	261	15
135.23888	-23.23713	81	45	135.19846	-23.10501	180	81
135.23888	-23.23713	90	56	135.09884	-23.09884	268	36
135.23947	-23.22404	84	51	135.16118	-22.98343	236	47
135.27559	-23.36785	14	30	135.15395	-23.00364	263	28
135.22842	-23.09967	5	80	135.16753	-23.09624	55	15
135.22698	-23.10543	30	78	135.16299	-23.09531	130	80
135.22808	-23.10638	35	75	135.15839	-23.09494	160	12
135.22953	-23.10698	40	80	135.10069	-23.09486	144	18
135.23347	-23.11127	208	80	135.08121	-23.10149	114	14
135.23795	-23.11335	214	80	135.07639	-23.10644	202	36
135.23942	-23.11487	227	72	135.0593	-23.14141	83	22
135.23858	-23.11672	234	54	135.22685	-23.03285	283	61
135.24258	-23.12095	310	17	135.22784	-23.03455	226	46
135.24442	-23.12145	20	68	135.22784	-23.03455	258	43
135.24705	-23.12272	0	1	135.22662	-23.03504	290	59
135.24705	-23.12272	160	1	135.22508	-23.03571	278	49
135.25392	-23.12178	285	26	135.2251	-23.03512	278	42
135.15751	-23.0477	245	29	135.22368	-23.03065	288	34
135.1581	-23.00286	255	44	135.2238	-23.02949	127	14
135.22645	-23.03278	252	46	135.22449	-23.02919	286	29
135.1865	-23.05482	242	38	135.2261	-23.02971	9	12
135.20863	-23.06095	277	38	135.22627	-23.02975	26	29
135.21777	-23.0565	230	58	135.22647	-23.03002	329	40
135.23803	-23.05657	270	43	135.22754	-23.03065	294	41
135.24728	-23.06467	285	42	135.22606	-23.03129	274	46
135.25277	-23.0709	340	45	135.15955	-22.97459	270	89
135.16148	-23.09473	155	72	135.16563	-22.98071	268	58
135.13757	-23.09353	200	32	135.16606	-22.98043	273	43
135.11578	-23.10213	155	32	135.1664	-22.98098	250	43
135.08005	-23.1021	220	14	135.17491	-22.98513	305	20
135.07523	-23.1057	80	42	135.17578	-22.98589	311	34
135.17647	-23.10747	195	18	135.2773	-23.07825	358	60
135.17472	-23.10752	180	31	135.27802	-23.07802	358	69
135.1728	-23.10828	60	20	135.27686	-23.07681	355	56
135.17325	-23.11058	65	18	135.27354	-23.07583	19	60
135.17475	-23.10973	180	24	135.27354	-23.07583	328	29
135.15956	-22.9746	272	76	135.28979	-23.08921	300	50
135.16556	-22.98072	245	42	135.29596	-23.10286	331	40
135.16556	-22.98072	28	42	135.26248	-23.0698	340	51
135.15869	-23.04809	47	22	135.25955	-23.06945	310	38
135.22685	-23.03379	124	30	135.1877	-23.05253	286	36
135.22803	-23.03443	54	60	135.18811	-23.05322	316	48
135.20805	-23.04235	80	43	135.14473	-22.98537	177	23
135.20964	-23.02833	84	29	135.14163	-22.98783	210	40
135.20911	-23.08394	90	28	135.159	-23.04841	242	29
135.20961	-23.09257	101	46	135.15846	-23.04839	270	32
135.16815	-23.09826	145	22	135.21503	-23.09085	223	50
135.16927	-23.10192	19	31	135.21503	-23.09085	264	25
135.17172	-23.09986	6	18	135.2139	-23.09062	240	33
135.17559	-23.10103	342	38	135.21272	-23.08966	283	29
135.18524	-23.08384	230	24	135.18582	-23.11094	103	11
135.18459	-23.0825	34	14	135.18573	-23.11113	222	22
135.18013	-23.07175	180	19	135.1859	-23.11258	300	10

135.29356	-23.09729	294	34	135.18604	-23.11543	166	10
135.28938	-23.08896	310	60	134.90935	-23.32015	206	41
135.31306	-23.13826	18	47	134.91324	-23.31923	176	36
135.2959	-23.10252	280	26	134.91295	-23.31774	218	22
135.23724	-23.1127	222	29	134.91724	-23.31278	180	20
135.23593	-23.11353	20	30	134.27634	-23.01386	152	84
135.23436	-23.1117	216	75	135.31477	-23.14333	329	73
135.23212	-23.11037	218	86	135.30464	-23.16829	30	29
135.23116	-23.10786	192	74	135.32272	-23.1824	303	21
135.23108	-23.10583	38	82	135.32758	-23.19092	274	51
135.23184	-23.10454	350	14	135.32578	-23.21247	29	44
135.23184	-23.10442	30	65	135.32518	-23.20719	76	61
135.23195	-23.10132	12	62	135.35674	-23.19855	8	31
135.22998	-23.09992	356	74	135.21524	-23.03391	283	35
135.22835	-23.09599	352	82	135.22789	-23.03326	267	71
135.22742	-23.09238	334	84	135.22789	-23.03326	294	41
135.29686	-23.12101	292	60	135.14951	-23.05483	195	37
135.29224	-23.09519	297	33	135.30522	-23.01637	355	34
135.29028	-23.09241	329	26	135.30537	-23.01975	316	31
135.28561	-23.08622	243	24	135.08025	-23.09524	200	30
135.28296	-23.08308	343	52	135.29612	-23.103	294	33
135.2809	-23.08055	10	82	135.07787	-23.0862	175	44
135.27687	-23.07687	348	46	135.07611	-23.08106	120	42
135.27353	-23.07585	16	60	135.18055	-23.07455	301	29

NUMERICAL MODEL

The model domain is 192 km tall and 384 km long with a grid resolution of 500 m, providing 294,912 elements populated with 17,694,720 particles. The uppermost layer is composed of sticky air, underlain by 2 km of sediments. Within the rift, sedimentary infill reaches a maximum of 34 km depth. Underneath the sediment, the basement reaches down to 40 km depth, atop an 80 km thick lithospheric mantle and a 48 km thick asthenospheric layer (Fig. 4A).

Materials are viscoplastic with properties dependent on stress, temperature, strain, and melt. We employ a scaled wet quartz rheology (Paterson and Luan, 1990) for the rift infill, reflecting the high melt and fluid content associated with metamorphism of the Harts Range Metamorphic Complex (HRMC). Plastic deformation follows a Drucker-Prager yield criterion, with materials weakening as plastic strain accumulates. The sediments within the rift are mechanically heterogenous, comprising weaker layers, stronger layers, and décollement layers. The rift infill density increases from 2400 kg m^{-3} at the surface to 2720 kg m^{-3} at the base, representing granulite-facies conditions (Daly et al., 1966). The basement density is set at a conservatively low density of 2820 kg m^{-3} , based on typical values used within gravity modelling within this region (e.g. Goleby et al., 1989). The material properties are summarized in Table DR4.

Radiogenic heat production within the basement and sediments ranges from Basement and sediments from 1.32×10^{-6} to $5 \times 10^{-6} \text{ W m}^{-3}$. The model permits a maximum melt fraction of 20% in the sediments and crust, and 3% in the mantle. Partial melt undergoes a viscosity reduction of 3 orders of magnitude in the sediments and crust, and 2 orders of magnitude in the mantle. The density of partially melted material drops by 13%.

A temperature anomaly of 1360° C is introduced, following a Gaussian distribution and reaching a depth of 65 km beneath the basin's left margin (Fig. 4A), which dissipates over time. The base of the model maintains a temperature of 1400° C , and the sticky air layer is fixed 15° C .

Boundary conditions are as follows: free slip on the top wall in both X and Y directions, free slip on the left and right walls in the Y direction with set velocities in the X direction. Initially, a background inflow velocity of 0.5 mm yr^{-1} is applied for the first 4 Myrs, followed by a gentle outflow velocity of 0.5 cm yr^{-1} up to 10 Myrs. The model base employs an Airy-like isostatic condition, maintaining constant pressure through asthenospheric inflow or outflow vertically in response to pressure changes (see Ibrahim and Rey, 2023)

The model script used to run this experiment is available at: <https://doi.org/10.5281/zenodo.8333247> or <https://github.com/JoeIbrahim/YIbrahim-Dome-to-Duplex>.

Table S 6. Material properties used in our numerical experiments. ε_1 and ε_2 refer to the accumulated plastic strain at which strain weakening begins and ceases, respectively.

Material	Reference Density (kg m^{-3}) ^a	ε_1	ε_2	Viscosity	Cohesion (MPa)	Weakened cohesion (Mpa)	Friction coefficient	Weakened friction coefficient
Sticky Air	1	NA	NA	10^{18} Pa s	NA	NA	NA	NA
Strong Sediments	2400-2720 ^b	0.0	0.15	0.1 * Wet Quartz	5	1	0.54	0.011
Weak Sediments				0.01 * Wet Quartz				
Décollement layers				10^{19} Pa s				
Basement	2820	0.0	0.15	Wet Quartz	15	1.5	0.54	0.011
Mantle	3370	NA	NA	Dry Olivine	NA	NA	NA	NA
Asthenosphere	3370	NA	NA	10^{20} Pa s	NA	NA	NA	NA

^aThermal expansivity of all materials is 2.8×10^{-5} . ^bSediment density increases with depth by 20 kg m^{-3} every 2 km.

References

- Crameri, F., Schmeling, H., Golabek, G.J., Duretz, T., Orendt, R., Buiter, S.J.H., May, D.A., Kaus, B.J.P., Gerya, T.V., and Tackley, P.J., 2012, A comparison of numerical surface topography calculations in geodynamic modelling: An evaluation of the “sticky air” method: Geophysical Journal International, v. 189, p. 38–54, doi:10.1111/j.1365-246X.2012.05388.x.
- Daly, R.A., Manger, G.E. and Clark, S.P., 1966. Section 4: Density of rocks. Geological Society of America Memoirs, 97, pp.19-26.
- Goleby, B.R., Shaw, R.D., Wright, C., Kennett, B.L.N., and Lambeck, K., 1989, Geophysical evidence for “thick-skinned” crustal deformation in central Australia: Nature, v. 337, p. 325–330, doi:10.1038/337325a0.
- Gonçalves, G. et al., 2015, An assessment of monazite from the Itambé pegmatite district for use as U–Pb isotope reference material for microanalysis and implications for the origin of the “Moacyr” monazite: Chemical Geology, v. 424, doi:10.1016/j.chemgeo.2015.12.019.
- Heaman, L.M., 2009, The application of U–Pb geochronology to mafic, ultramafic and alkaline rocks: An evaluation of three mineral standards: Chemical Geology, v. 261, p. 43–52, doi:10.1016/j.chemgeo.2008.10.021.

Horstwood, M.S.A., Foster, G.L., Parrish, R.R., Noble, S.R., and Nowell, G.M., 2003, Common-Pb corrected in situ U–Pb accessory mineral geochronology by LA-MC-ICP-MS: *Journal of Analytical Atomic Spectrometry*, v. 18, p. 837–846, doi:10.1039/B304365G.

Hurai, V., Paquette, J.-L., Huraiová, M., and Konečný, P., 2010, U–Th–Pb geochronology of zircon and monazite from syenite and pincinite xenoliths in Pliocene alkali basalts of the intra-Carpathian back-arc basin: *Journal of Volcanology and Geothermal Research*, v. 198, p. 275–287, doi:10.1016/j.jvolgeores.2010.09.012.

Ibrahim, Y., and Rey, P.F., 2023, The Role of Isostasy in the Evolution and Architecture of Fold and Thrust Belts (F. Cheng, Ed.): *Lithosphere*, v. 2023, p. 8503619, doi:10.2113/2023/8503619.

Müller, W., Shelley, M., Miller, P., and Broude, S., 2009, Initial performance metrics of a new custom-designed ArF excimer LA-ICPMS system coupled to a two-volume laser-ablation cell: *Journal of Analytical Atomic Spectrometry*, v. 24, p. 209–214, doi:10.1039/B805995K.

Paterson, M.S., and Luan, F.C., 1990, Quartzite rheology under geological conditions: *Geological Society Special Publication*, v. 54, p. 307, doi:10.1144/GSL.SP.1990.054.01.26.

Paquette, J.-L., Piro, J.L., Devidal, J.L., Bosse, V., Didier, A., Sannac, S., and Abdnour, Y., 2014, Sensitivity Enhancement in LA-ICP-MS by N₂ Addition to Carrier Gas: Application to Radiometric Dating of U-Th-Bearing Minerals: *Agilent ICP-MS J.*, v. 58.

Paquette, J.L., and Tiepolo, M., 2007, High resolution (5 μm) U–Th–Pb isotope dating of monazite with excimer laser ablation (ELA)-ICPMS: *Chemical Geology*, v. 240, p. 222–237, doi:10.1016/j.chemgeo.2007.02.014.

Spandler, C., Hammerli, J., Sha, P., Hilbert-Wolf, H., Hu, Y., Roberts, E., and Schmitz, M., 2016, MKED1: a new titanite standard for in situ analysis of Sm–Nd isotopes and U–Pb geochronology: *Chemical Geology*, v. 425, p. 110–126, doi:10.1016/j.chemgeo.2016.01.002.

Tomascak, P.B., Krogstad, E.J., and Walker, R.J., 1996, U–Pb Monazite Geochronology of Granitic Rocks from Maine: Implications for Late Paleozoic Tectonics in the Northern Appalachians: *The Journal of Geology*, v. 104, p. 185–195.

van Achterberg, E., Ryan, C., Jackson, S., and Griffin, W., 2001, Data reduction software for LA-ICP-MS: Laser Ablation ICP-MS in the Earth Science, *Mineralogical Association of Canada*, v. 29, p. 239–243.

Wiedenbeck, M., Allé, P., Corfu, F., Griffin, W. l., Meier, M., Oberli, F., Quadt, A.V., Roddick, J. c., and Spiegel, W., 1995, Three Natural Zircon Standards for U-Th-Pb, Lu-Hf, Trace Element and Ree Analyses: *Geostandards Newsletter*, v. 19, p. 1–23, doi:10.1111/j.1751-908X.1995.tb00147.x.